Research Article

Evaluation of the Antiproliferative Properties of CpRu Complexes Containing N-Methylated Triazaphosphaadamantane Derivatives

Andres Alguacil [ID],[1] Franco Scalambra [ID],[1] Antonio Romerosa [ID],[1] Andreia Bento-Oliveira,[2] Fernanda Marques [ID],[3] Ines Maximiano,[2] Rodrigo F. M. de Almeida [ID],[2] Ana Isabel Tomaz [ID],[2] and Andreia Valente [ID][2]

[1]*Área de Química Inorgánica–CIESOL, Universidad de Almería, Almería 04120, Spain*
[2]*Centro de Química Estrutural, Institute of Molecular Sciences, Departamento de Química e Bioquímica, Faculdade de Ciências, Universidade de Lisboa, Campo Grande 1749-016, Lisboa, Portugal*
[3]*Centro de Ciências e Tecnologias Nucleares e Departamento de Engenharia e Ciências Nculeares, Instituto Superior Técnico (C2TN/IST), Universidade de Lisboa, Estrada Nacional 10, Bobadela LRS 2695-066, Portugal*

Correspondence should be addressed to Antonio Romerosa; romerosa@ual.es and Andreia Valente; amvalente@ciencias.ulisboa.pt

Piano-stool-{CpRu} complexes containing 1,3,5-triaza-7-phosphaadamantane (PTA), *N*-methyl-1,3,5-triaza-7-phosphaadamantane (mPTA), and 3,7-dimethyl-1,3,7-triaza-5-phosphabyciclo[3.3.1]nonane (dmoPTA) were evaluated as drugs against breast cancer. The evaluated compounds include two new examples of this family, the complexes $[RuCp(DMSO-\kappa S)(HdmoPTA)(PPh_3)](CF_3SO_3)_2$ (**8**) and $[RuCp(PPh_3)_2-\mu\text{-}dmoPTA\text{-}1\kappa P\text{-}2\kappa^2 N,N'\text{-}PdCl_2](CF_3SO_3)$ (**11**), which have been synthesized and characterized by NMR, IR, and single-crystal X-ray diffraction. The cytotoxic activity of compounds was evaluated against MDA-MB-231 breast cancer cells, and the three most active complexes were further tested against the hormone-dependent MCF-7 breast cancer cell line. Their cell death mechanism and ruthenium uptake were also evaluated, as well as their binding ability to human serum albumin.

1. Introduction

The development of new drugs for the treatment of cancer is certainly a topic of preeminent importance. Since the discovery of the anticancer activity of *cis*-$[PtCl_2(NH_3)_2]$ (cisplatin) by Rosenberg et al. in the 1960s [1, 2], large research efforts have been focused on the development of new platinum-based drugs, some of which are currently used in numerous chemotherapeutic treatments [3–5]. However, their side effects, lack of selectivity, and resistance-related issues pushed the scientific community to explore complexes with similar geometry and chemical properties but containing other metals such as Pd(II) [6–8]. This strategy has led to the recent regulatory approval in Europe of the Pd-porphyrin complex padeliporfin (WST11) for photodynamic therapy treatments [9].

Research efforts targeted to obtain alternatives to Pt(II) compounds have led to the development of new complexes containing metals that adopt different coordination geometries concerning the strictly square planar of Pt(II) and Pd(II). Among the transition metals that meet this requirement, ruthenium is one of the most promising [10–12]. Several ruthenium-based compounds have shown outstanding encouraging results such as Ru(III) complexes KP1019 (replaced by NKP1339/IT-139) and NAMI-A, which entered phases I and II of clinical trials, respectively [12]. Other examples are the Ru(II) complex TLD1433, which was evaluated in phase II [13, 14], and the compounds
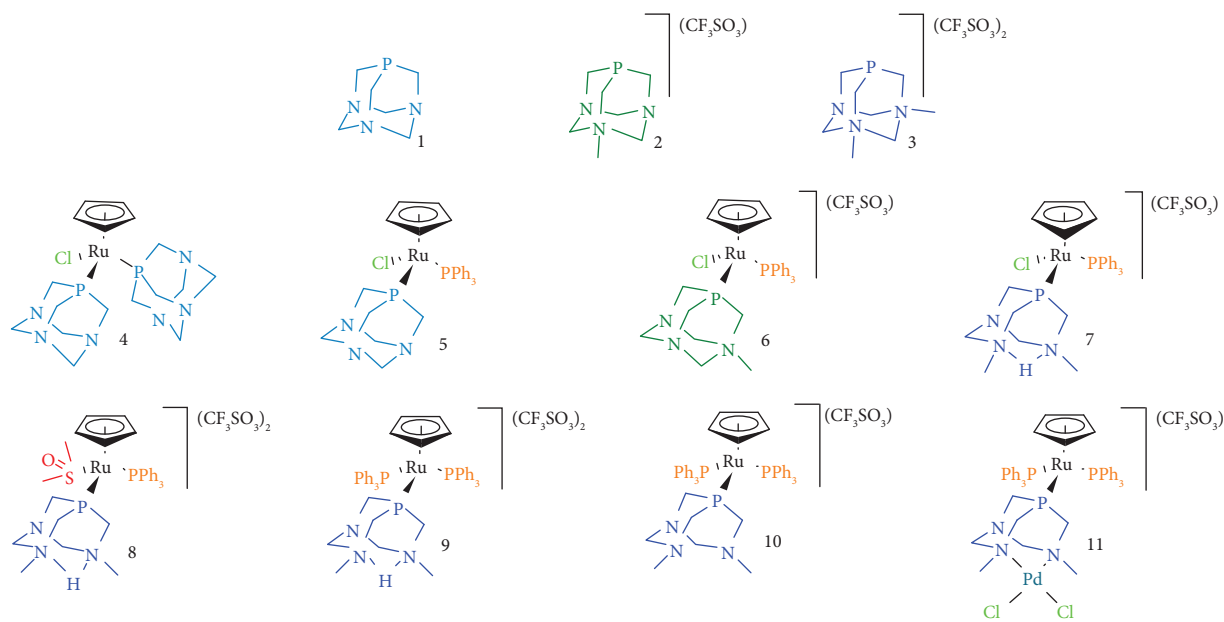
FIGURE 1: PTA-type ligands (**1**–**3**) and their RuCp complexes (**4**–**11**) were studied in this work and screened for their anticancer activity in the breast model.

of the family of RAPTAs, which were tested in preclinical trials [15–17]. This latter group of complexes exhibits a Ru-(η^6-arene) scaffold and 1,3,5-triaza-7-phosphaadamantane (PTA, **1**) together with two chlorides (Figure 1) [18]. The combination of ligands and their arrangement around the metal provides a stable platform with adequate hydrosolubility, stabilizing the Ru(II) oxidation state [19].

To date, and inspired by the RAPTA family, a discrete number of antiproliferative ruthenium compounds bearing PTA and derivatives have been synthesized [20–22]. In this line, complexes containing 3,7-dimethyl-1,3,7-triaza-5-phosphabicyclo[3.3.1]nonane (dmoPTA), which is a hydrolysis product of N,N′-dimethyl-1,3,5-triaza-7-phosphaadamantane (dmPTA) (**3**, Figure 1), display a very good antiproliferative profile [23], surpassing the activity of cisplatin up to 200 times in some cases [24]. Some of the most active examples of this family of compounds are heterometallic complexes in which the dmoPTA ligand is binding ruthenium by the phosphorus atom and chelates harder metals through methylated nitrogens [24–29], and have been studied along with other complexes presented in this work together with the free ligands by ^{15}N NMR. [30].

The reasons that determine the significant cytotoxic activity of heterometallic complexes containing dmoPTA are not still envisaged. As a part of our efforts to shed light on this topic, some significantly active previously published complexes containing PTA and PTA derivatives (Figure 1) were compared with the two new members of this family: monometallic [RuCp(DMSO-κS)(HdmoPTA)(PPh$_3$)](CF$_3$SO$_3$)$_2$ (**8**) and bimetallic [RuCp(PPh$_3$)$_2$-μ-dmoPTA-1κP-2κ^2N,N′-PdCl$_2$] (CF$_3$SO$_3$) (**11**). Complexes **1**–**11** were evaluated against the MDA-MB-231 breast cancer cell line, and the most active compounds (**9**–**11**) were further tested against the MCF-7 breast cancer cell line. In addition, their cell death mechanism and cell distribution (Ru quantification) were

also determined. To gain insight into the possible role of human serum albumin (HSA) in their bloodstream distribution, their interaction with HSA was also quantified using steady-state and time-resolved fluorescence.

2. Experimental

2.1. Materials and Methods. All chemicals were reagent grade and, unless otherwise stated, were used as received by commercial suppliers. In the synthesis of the new compounds, all solvents used were degassed and distilled according to standard procedures. All reactions and manipulations were routinely performed under a dry nitrogen atmosphere using standard Schlenk-tube techniques. Hydrosoluble phosphines PTA (**1**) [18], mPTA(CF$_3$SO$_3$) (**2**) [31], and dmPTA(CF$_3$SO$_3$)$_2$ (**3**) [23] and complexes [RuClCp(PTA)$_2$] (**4**) [32], [RuClCp(PPh$_3$) (PTA)] (**5**) [31], [RuClCp(PPh$_3$)(mPTA)](CF$_3$SO$_3$) (**6**) [31], [RuClCp(HdmoPTA)(PPh$_3$)](CF$_3$SO$_3$) (**7**) [23], [RuCp(Hdmo PTA)(PPh$_3$)$_2$](CF$_3$SO$_3$)$_2$ (**9**) [27], and [RuCp(dmoPTA)(PPh$_3$) $_2$](CF$_3$SO$_3$) (**10**) [24] were prepared as described in the literature. ^{1}H, ^{13}C{^{1}H}, and ^{31}P{^{1}H} NMR spectra were recorded on a Bruker DRX500 spectrometer operating at 500.13 MHz, 150.77 MHz, and 202.46 MHz, respectively. Peak positions are relative to tetramethylsilane and were calibrated against the residual solvent resonance (^{1}H) or the deuterated solvent multiplet (^{13}C). Chemical shifts for ^{31}P{^{1}H} NMR were measured relative to external 85% H$_3$PO$_4$ with downfield values taken as positive. Elemental analysis (C, H, N, S) was performed on a Fisons Instruments EA 1108 elemental analyser. Infrared spectra have been carried out on a Bruker ECO-ATR ALPHA spectrometer, and the intensity of the bands has been indicated as strong (s), medium (m), and weak (w). The electronic absorption spectra were acquired on Jasco UV-1603 or a Jasco V-560 spectrophotometer (JASCO, Hiroshima, Japan) at room temperature with 1 cm optical path quartz Hellma cuvettes. The

solubility of the synthesized complexes was determined by UV-vis spectrophotometry techniques. Fluorescence measurements were performed on a Fluorolog 3.22 spectrofluorometer from Horiba Jobin Yvon (Villeneuve D'ascq, France) at $(25.0 \pm 0.1)°C$.

2.2. Synthetic Procedures

2.2.1. Synthesis of [RuCp(DMSO-κS)(HdmoPTA)(PPh₃)](CF₃SO₃)₂

2.2.1. Synthesis of [RuCp(DMSO-κS)(HdmoPTA)(PPh₃)](CF₃SO₃)₂ (8). 32.6 mg of AgCF₃SO₃ (0.127 mmol) was added into a solution of 50 mg of [RuClCp(HdmoPTA)(PPh₃)](CF₃SO₃) (7) (0.0635 mmol) in 0.5 mL of DMSO. A white AgCl precipitate was formed, and the mixture was stirred for 24 h, filtered with celite, and washed with 1 mL of EtOH. 5 mL of Et₂O was added to the filtered solution, and a whitish precipitate appeared. It was filtered and washed with Et₂O (3 × 3 mL) and left to dry under vacuum. Yield: 53.5 mg, 86%. Solubility: $S_{25°C,acetone}$ 40.8 mg/cm³, $S_{25°C,MeOH}$ 19.2 mg/cm³, and $S_{25°C,DMSO}$ 76.4 mg/cm³. $C_{34}H_{43}F_6N_3O_7P_2RuS_3$ (979.07 g·mol⁻¹). Calcd: C 41.67; H 4.26; N 4.29; S 9.79. Found: C 41.27; H 4.52; N 4.47; S 9.51. IR: 1438 (w), 1252 (s), 1226 (m), 1151 (m), 1097 (w), 1033 (s), 997 (m), 934 (m), 756 (m), 704 (m), 698 (m), and 641 (s). ¹H NMR (500.13 MHz, acetone-d₆, 25°C) δ (ppm): 2.50 + 2.54 $(d + d, {}^2J_{HH} = 1.46$ Hz, ${}^2J_{HH} = 1.44$ Hz, 3H + 3H, $CH_3NCH_2P_{HdmoPTA}$), 3.01 + 3.67 $(s + s, 3H + 3H, (CH_3)_2SO)$, 3.42–3.66 + 4.30 $(m + m, 6H, NCH_2P_{HdmoPTA})$, 4.02 + 4.51 $(d + m, {}^2J_{HH} = 11.61$ Hz, 4H, $NCH_2N_{HdmoPTA})$, 5.44 (s, 5H, Cp), and 7.56–7.67 (m, 15H, PPh₃). ¹³C{¹H} NMR (125.76 MHz, acetone-d₆, 25°C) δ (ppm): 42.31 + 42.45 $(d + d, {}^3J_{PC} = 5.24$ Hz, ${}^3J_{PC} = 4.93$ Hz, $CH_3NCH_2P_{HdmoPTA})$, 54.23 + 58.98 $(s + s, (CH_3)_2SO)$, 48.16 + 48.34 + 55.68 + 55.85 + 56.24 + 56.40 $(m + m + m + m, NCH_2P_{HdmoPTA})$, 74.97 + 75.05 $(d + d, {}^3J_{PC} = 3.74$ Hz, ${}^3J_{PC} = 3.20$ Hz, $NCH_2N_{HdmoPTA})$, 85.72 (s, Cp), and 129.16–133.90 (m, PPh₃). ³¹P{¹H} NMR (202.46 MHz, acetone-d₆, 25°C) δ (ppm): −5.89 (d, ${}^2J_{PP} = 37.64$ Hz, HdmoPTA), and 41.48 (d, ${}^2J_{PP} = 37.45$ Hz, PPh₃).

2.2.2. Synthesis of [RuCp(PPh₃)₂-μ-dmoPTA-1κP-2κ²N,N′-PdCl₂](CF₃SO₃) (11). (NBu₄)₂[PdCl₄] (68 mg, 0.098 mmol) was added into a solution of [RuCp(PPh₃)₂(dmoPTA)](CF₃SO₃) (10) (100 mg, 0.098 mmol) in dry MeOH (20 mL). The mixture was stirred at room temperature for 30 minutes, and the solvent was removed. The pale brown residue was dissolved in CHCl₃ (10 mL), and it was filtered by gravity. The filtered dissolution was concentrated under reduced pressure, and Et₂O was added drop to drop until a pale brown precipitate was observed. The resulting precipitate was suction filtered, washed with Et₂O (3 × 20 mL), and dried under vacuum. Yield: 62.9 mg, 54%. Solubility: $S_{25°C,CHCl3}$ 4.8 mg/cm³, $S_{25°C,DMF}$ 17 mg/cm³, and $S_{25°C,DMSO}$ 25.2 mg/cm³. $C_{49}H_{51}Cl_2F_3N_3O_3P_3PdRuS$ (1189,03 g·mol⁻¹). Calcd: C 49.45; H 4.32; N 3.53; S 2.69. Found: C 49.64; H 4.47; N 3.39; S 2.48. IR: 2958 (w); 1433 (m); 1275 (s), 1158 (s); 826 (s). ¹H NMR (600.13 MHz, CDCl₃, 25°C) δ (ppm): 2.45 (s, 6H, NCH_3), 3.10 + 4.01 $(m + m, 4H, PCH_2NCH_3)$, 3.45 (m, 2H, PCH_2N), 4.24 (m, 4H, NCH_2N), 5.16 (s, 5H, Cp), and 6.89–7.60 ppm (m, 30 H, aromatics, PPh₃). ¹³C{¹H} NMR (150.90 MHz, CDCl₃, 25°C) δ (ppm): 53.04 (m, NCH_3), 60.27 (m, PCH_2N), 61.77 (m, PCH_2NCH3), 78.25

(m, NCH_2N), 86.50 (s, Cp), and 128.45–136.51 (PPh₃). ³¹P{¹H} NMR (242.94 MHz, CDCl₃, 20°C) δ (ppm): −10.48 (m, dmoPTA-PdCl₂), and 39.51 (d, ${}^2J_{PP} = 38.92$ Hz, PPh₃).

2.3. Single-Crystal X-Ray Diffraction

2.3. Single-Crystal X-Ray Diffraction. Single crystals of **8** and **11** were obtained by evaporation of acetone and CHCl₃ solutions, respectively. Single-crystal X-ray diffraction measurements were performed with a Bruker APEX-II CCD diffractometer using MoKα radiation. Data were integrated (SAINT, Bruker) and scaled (SADABS, Bruker), and finally, the structure was solved with SHELXT using intrinsic phasing and refined with SHELXL by least squares [33, 34]. Solution and refinement procedures were accomplished by using Olex2 software [35]. The crystal structures of **8** and **11** have been deposited at CSD with CCDC numbers 2263437 (**8**) and 2261422 (**11**). The crystallographic and experimental parameters are summarized in Table S1. Distances and angles are summarized in Tables S2–S6.

2.4. Biological Evaluation

2.4.1. Stability Studies

2.4.1. Stability Studies. The assessment of the biological properties of the complexes requires their dissolution in a cell culture medium which is mainly constituted by water. When the complex is not hydrosoluble enough, the used protocol contemplates preliminary dissolution in DMSO before the addition to the culture medium [36]. Thus, it is important to determine the stability and behaviour of the complexes in both DMSO and water/DMSO mixtures to check whether different species have been formed when dissolved. Dissolutions in DMSO-d₆ and DMSO-d₆/D₂O of the new complexes **8** and **11** were monitored by ³¹P{¹H} NMR over time at room temperature and 37°C. The stability studies of the rest of the complexes (1-7, 9, 10) were published previously. All experiments were performed by a similar procedure: the complex (0.01 g) was introduced into a 5 mm NMR tube and dissolved in 0.5 mL of degassed solvent (DMSO-d₆ and a 1 : 1 mixture of DMSO-d₆/D₂O). The solution was left at room temperature and monitored by ³¹P{¹H} NMR first every 15 minutes, and later in longer periods. Stability was also monitored at incubation cell-based assay temperature (37°C).

2.4.2. Cell Lines and Culture Conditions

2.4.2. Cell Lines and Culture Conditions. The MDA-MB-231 and MCF-7 human breast cancer cells were purchased from ATCC. The MDA-MB-231 and MCF-7 cells were grown in Dulbecco's modified Eagles' medium (DMEM high glucose) (Capricorn Scientific) at 37°C in 5% CO₂ supplemented with 10% fetal bovine serum (Capricorn Scientific). HDF cells were purchased from Merck and were grown in the fibroblast growth medium. All cells were adherent in monolayers and, upon confluence, were washed with phosphate buffer saline (PBS) and harvested by digestion with trypsin-EDTA 0.05% (v/v). The cells were suspended and transferred into new, sterile, culture flasks for maintenance or seeded in sterile test microplates for different assays. All cells were manipulated under aseptic conditions in a flow chamber.

2.4.3. Compound Cytotoxicity Evaluated Using the MTT Assay.

The cells were adherent in monolayers and, upon confluence, were harvested by digestion with trypsin. The cytotoxicity of the complexes against the tumour cells was assessed using the colorimetric assay MTT (3-(4,5-2-yl)-2,5-ditetrazolium bromide), which evaluates the metabolic activity of viable cells. This assay measures the conversion of yellow tetrazolium into purple formazan by an active mitochondrial dehydrogenase in living cells. For this purpose, the cells ($10{-}20 \times 10^3$ in $200 \, \mu L$ of the medium) were seeded into 96-well plates and incubated in a 5% CO_2 incubator at $37°C$. The cells were settled for 24 h followed by the addition of a dilution series of the complexes in a medium ($200 \, \mu L$). The complexes were first solubilized in 100% DMSO, given a 10 mM stock solution, and then in a medium within the concentration range of $0.1{-}100 \, \mu M$. DMSO did not exceed 1% even for the higher concentration used and was without cytotoxic effects. After 24 h of incubation, the treatment solutions were removed by aspiration, and MTT solution ($200 \, \mu L$, $0.5 \, mg \cdot mL^{-1}$ in PBS) was added to each well. After 3 h at $37°C/5\%$ CO_2, the solution was removed, and the purple formazan crystals formed inside the cells were dissolved in DMSO ($200 \, \mu L$) by thorough shaking. The cellular viability was evaluated by measuring the absorbance at 570 nm by using a microplate spectrophotometer. The IC_{50} values were obtained by dose-response curves using the GraphPad Prism software (vs. 5).

2.4.4. Cell Death Measurement Using Flow Cytometry: The Annexin V/PI Assay.

After 24 h treatment with compounds **9**, **10**, and **11**, both suspended and attached cells were collected and washed with PBS. The cells were resuspended in $200 \, \mu L$ of 1x binding buffer and were incubated with $5 \, \mu L$ of FITC annexin V (BD Biosciences, San Jose, CA, USA) and $10 \, \mu L$ of PI ($50 \, mg \cdot mL^{-1}$) for 20 min in the dark. The samples were analysed by using fluorescence-activated cell sorting (FACS) using Beckman Coulter EPICS XL-MCL. All data were analysed using the FlowJo software (version 10, Tree Star Inc.).

2.4.5. Complex Uptake and Distribution by ICP-MS.

For the cellular uptake experiments, MDA-MB-231 cells (approx. $5 \cdot 10^6$ cells/5 mL medium) were exposed to the complexes at their respective IC_{50} concentrations and in two conditions (6 h and 24 h of incubation time) and then washed with ice-cold PBS and centrifuged to obtain a cellular pellet [37]. The cytosol, membrane/particulate, cytoskeletal, and nuclear fractions were extracted using a FractionPREP™ cell fractionation system (BioVision, USA) and performed according to the manufacturer's protocol. The Ru (^{101}Ru) and Pd (^{106}Pd) contents in different fractions were measured by using Thermo X-Series Quadrupole ICP-MS (Thermo Scientific) after the digestion of the samples. Briefly, the samples were digested with ultrapure HNO_3 (65%), H_2O_2, and H_3PO_4 in a closed pressurized microwave digestion unit (Mars5, CEM) with medium-pressure HP500 vessels and then diluted in ultrapure water to obtain 2.0% (v/v) nitric acid. The instrument was tuned using a multielement ICP-MS 71C standard solution (Inorganic Venture). Indium (115In) at $10 \mu ML^{-1}$ was used as the internal standard.

2.4.6. Interaction with Human Serum Albumin.

The stock solutions of HSA were freshly prepared for each experiment by gently dissolving protein in PBS pH 7.4 (tablets from Fisher) for 1 hour to allow protein to completely hydrate. The concentration of the protein in the stock solutions was determined by spectrophotometry using the molar absorption coefficient at 280 nm ε_{280}(HSA) = 36,850 $M^{-1} \cdot cm^{-1}$ [38].

In each essay, all spectroscopic measurements were carried out on individually prepared samples to ensure the same preincubation time at $(37.0 \pm 0.1)°C$, the same % of DMSO in the final samples, and the same exposure to excitation light and to avoid the need for dilution corrections. Moreover, for a direct titration protocol, a highly concentrated stock solution of the compounds in the buffer would be required, which would raise solubility issues. Dimethylsulfoxide (DMSO, from Fisher) was used to prepare concentrated stock solutions of each complex, followed by appropriate dilution to obtain the desired concentration. The DMSO content was kept at 2% (v/v) in PBS pH 7.4 in all samples. Dilutions were carried out immediately before sample preparation.

Fluorescence measurements were performed at $25.0 \pm 0.1°C$. The final protein concentration in the individually prepared samples (3.72 to $5 \, \mu M$) was kept constant in each assay, and the complex concentration was varied to obtain desired HSA: Ru-complex molar ratios ranging from $1:0.25$ to $1:10$. A control sample containing the same amount of protein and final DMSO content and with no complex was also prepared for each experiment. Appropriate blank samples with no protein but with the same complex concentrations were prepared as well for background correction.

The steady-state fluorescence intensity was measured with excitation at 295 nm, and emission spectra were collected with bandwidths of 4 nm for both excitation and emission. For Stern–Volmer plots, the fluorescence intensity with emission at 340 nm was selected because it is near the maximum emission wavelength (so the sensitivity is close to maximum), but it is further to red in relation to the water Raman scattering peak [39]. These values were corrected for the absorption and emission inner filter effects [40] using the absorbance recorded for each sample at the excitation and emission wavelengths used for the steady-state quenching analysis. For time-resolved fluorescence measurements, the single-photon-counting technique was used with nanoLED N-280 (Horiba Jobin Yvon) as the pulsed excitation source (280 nm) and with emission collected at 350 nm (13 nm emission bandwidth), eliminating the contribution of the emission by tyrosine residues.

The experimental fluorescence intensity decays of HSA in buffer solution can be described by a sum of exponentials:

$$I(t) = \sum_{i=1}^{n} p_i \exp\left(-\frac{t}{\tau_i}\right), \tag{1}$$

where p_i and τ_i are the pre-exponential factors and lifetime of component i, respectively. The amplitude or normalized pre-exponential of each lifetime component α_i is $p_i/\Sigma_i p_i$ with $\Sigma_i \alpha_i = 1$. Fluorescence decays were analysed by an iterative

deconvolution method using the *TRFA Data Processor software* (version 1.4; Minsk, Belarus), and the instrument response function was obtained using scattering by a colloidal suspension of silica (Ludox®, Sigma-Aldrich) diluted in water. Criteria for judging the quality of the fit were reduced χ^2 close to 1 and a random distribution of weighted residuals and residual autocorrelation.

To evaluate changes in the quantum yield by processes affecting the fluorescence lifetimes of HSA, the *amplitude-weighted mean fluorescence lifetime* ($\overline{\tau}$) was calculated using the following equation:

$$\overline{\tau} = \sum_{i=1}^{n} \alpha_i \tau_i. \qquad (2)$$

3. Results and Discussion

3.1. Characterization of Complexes 8 and 11. The complex [RuCp(DMSO-κS)(HdmoPTA)(PPh$_3$)](CF$_3$SO$_3$)$_2$ (**8**) was synthesized by addition of AgCF$_3$SO$_3$ into a solution of **7** in DMSO (Scheme 1(a)), while the complex [RuCp(PPh$_3$)$_2$-μ-dmoPTA-1κP-2$\kappa^2 N,N'$-PdCl$_2$](CF$_3$SO$_3$) (**11**) was obtained (Scheme 1(b)) by reaction in methanol of (NBu$_4$)$_2$[PdCl$_4$] with [RuCp(PPh$_3$)$_2$(dmoPTA)](CF$_3$SO$_3$) (**10**) [24]. These complexes were obtained as whitish and pale brown solids, respectively, in moderate to good yield, and were characterized in the solid state (FTIR, XRD, and elemental analysis) and solution (^{1}H, ^{31}P{^{1}H}- NMR, ^{13}C{^{1}H} NMR, and 2D NMR)–see supporting information for details (Figures S1–S6 for **8** and Figures S7–S12 for **11**).

At 25°C, complex **8** is soluble in MeOH (19.2 mg/cm^3), acetone (40.8 mg/cm^3), and DMSO (76.4 mg/cm^3), while **11** is soluble in CHCl$_3$ (4.8 mg/cm^3), DMF (17 mg/cm^3), and DMSO (25.2 mg/cm^3). The ^{1}H NMR resonances were assigned with the help of ^{1}H-^{1}H COSY and ^{1}H-^{13}C HSQC experiments (**8**: Figures S5-S6; **11**: Figures S11-S12), which are in agreement with the crystal structure of the complexes and display similar chemical shifts than those found for similar compounds [24, 28, 41]. It is interesting to point out that the ^{1}H NMR spectrum of **8** shows the distinctive signals of κS-coordinated DMSO (δ (ppm, acetone-d$_6$) = 3.01 + 3.67, $s + s$), while no evidence for the κO-DMSO coordination was observed [26–28]. The ^{31}P{^{1}H} NMR spectra of **8** and **11** display the signal of PPh$_3$ as a doublet (**8**: 41.48 ppm ($^2 J_{PP}$ = 37.45 Hz), acetone-d$_6$; **11**: 39.51 ppm ($^2 J_{PP}$ = 38.92 Hz), CDCl$_3$), while that of the dmoPTA ligand appears as a doublet in the spectra of **8** (−5.89 ppm, acetone-d$_6$) and a triplet for **11** (−10.48 ppm, CDCl$_3$), agreeing to those observed in analogue complexes and with their crystal structure [24, 28, 41]. CF$_3$SO$_3^-$ counterions in both complexes were confirmed by ^{13}C{^{1}H} NMR and IR (**8**: ν_{SO3} = 1252 cm^{-1}; **11**: ν_{SO3} = 1275 cm^{-1}).

The asymmetric unit of **8** is constituted by the cationic complex [RuCp(DMSO-κS)(HdmoPTA)(PPh$_3$)]$^{2+}$, two triflate counterions, and one molecule of acetone, while the asymmetric unit of **11** contains one bimetallic cationic complex [RuCp(PPh$_3$)$_2$-μ-dmoPTA-1κP-2$\kappa^2 N,N'$-PdCl$_2$]$^+$ (Figure 2), one disordered triflate, and four molecules of CHCl$_3$. The coordination sphere around the Ru atom in both complexes shows the expected distorted pseudooctahedral geometry. The Ru-Cp$_{centroid}$ distance (**8**: 1.887·Å; **11**: 1.885·Å) is similar to that found in similar complexes [23–28, 41]. The angle between the Cp plane and the P1-Ru1-P2 plane is 51.24° for **8** and 49.14° for **11**, which are slightly smaller than those found in [RuCp(PPh$_3$)$_2$-μ-dmoPTA-1κP-2$\kappa^2 N,N'$-ZnCl$_2$] (CF$_3$SO$_3$) (51.20°), [RuCp(PPh$_3$)$_2$-μ-dmoPTA-1κP-2$\kappa^2 N,N'$-CoCl$_2$](CF$_3$SO$_3$) (52.85°), and [RuCp(DMSO-κS)(PPh$_3$) (PTA)](CF$_3$SO$_3$) (52.82°) [24, 28, 41].

Bond lengths between ruthenium and P$_{dmoPTA}$ in **8** and **11** are almost identical (**8**: Ru1-P1 = 2.3107(8) Å; **11**: Ru1-P1 = 2.3077(5) Å) and slightly shorter than those in similar previously reported complexes (**9**: 2.321(1) Å; **10**: 2.319(1) Å; [RuCp(PPh$_3$)$_2$-μ-dmoPTA-1κP-2$\kappa^2 N,N'$-ZnCl$_2$](CF$_3$SO$_3$): 2.327(1) Å) [24, 27]. The Ru-P$_{PPh3}$ bond length for **8** was found to be a bit longer (2.3635(9) Å) than that in [RuCp(DMSO-κS)(PPh$_3$)(PTA)](CF$_3$SO$_3$) (2.333(1) Å) [41]. Bimetallic complex **11** displays somewhat larger Ru-P$_{PPh3}$ bond lengths (Ru1-P2 = 2.3717(6) Å; Ru1-P3 = 2.3650(5) Å) than **8**, which are similar to those previously reported for complex **9** (Ru1-P2 = 2.366(1) Å; Ru1-P3 = 2.389(1) Å) and Ru-Zn complex [RuCp(PPh$_3$)$_2$-μ-dmoPTA-1κP-2$\kappa^2 N,N'$-ZnCl$_2$](CF$_3$SO$_3$) (Ru1-P2 = 2.377(1) Å; Ru1-P3 = 2.388(1) Å) [24, 27]. The Ru1-S1 bond length in **8** is 2.2764(9) Å, in agreement with analogous Ru(II)-κS-DMSO complexes such as [RuCp(DMSO-κS)(PPh$_3$)(PTA)](CF$_3$SO$_3$) (2.2616(8) Å) [41].

The palladium atom in **11** is surrounded by the two CH$_3$N$_{dmoPTA}$ atoms and two chlorides in a distorted square planar geometry (N1-Pd1-N2 = 88.12(7)°; Cl1-Pd1-Cl2 = 85.25(2)°; N1-Pd1-Cl1 = 93.68(5)°; N2-Pd1-Cl2 = 92.96(5)°). The Pd-Cl and Pd-N bond lengths (Pd1-Cl1 = 2.2876(6) Å; Pd1-Cl2 = 2.3059(6) Å; Pd1-N1 = 2.1092(18) Å; Pd1-N2 = 2.1058(19) Å) are close to the typical bond distances in the structure of similar complexes such as *cis*-[PdCl$_2$(NH$_3$)$_2$] (Pd1-Cl1 = 2.26(2) Å; Pd1-Cl2 = 2.29(2) Å; Pd1-N1 = 1.99(4) Å; Pd1-N2 = 2.13(4) Å) [42] and *trans*-[PdCl$_2$(NH$_3$)$_2$] (Pd1-Cl1 = 2.277(2) Å; Pd1-Cl2 = 2.294(2) Å; Pd1-N1 = 2.115(9) Å; Pd1-N2 = 2.097(9) Å) [43]. Finally, the crystal packing of both complexes does not show significant interactions such as π-π stacking or hydrogen bonding.

3.2. Biological Evaluation

3.2.1. Stability Studies. The stability of RuCp complexes in DMSO and in DMSO/H$_2$O mixtures has been studied quite extensively in recent years. In general, this family of complexes is reasonably stable in the abovementioned solvent mixtures, and in most cases, decomposition occurs at longer times in comparison with the antiproliferative assays. Nevertheless, typical decomposition pathways usually involve the release of ligands Cl$^-$ or PPh$_3$, which are substituted by solvent molecules (H$_2$O or DMSO) [24, 26, 28].

Complex **8** is soluble in DMSO-d$_6$ and DMSO-d$_6$/D$_2$O (1 : 1) and stable in both media at room temperature and at 37°C as no spectral changes were observed during 48 h (Figures S13–S16 in S.I.). Also, complex **11** is very stable in DMSO-d$_6$ at room temperature and 37°C showing two sharp
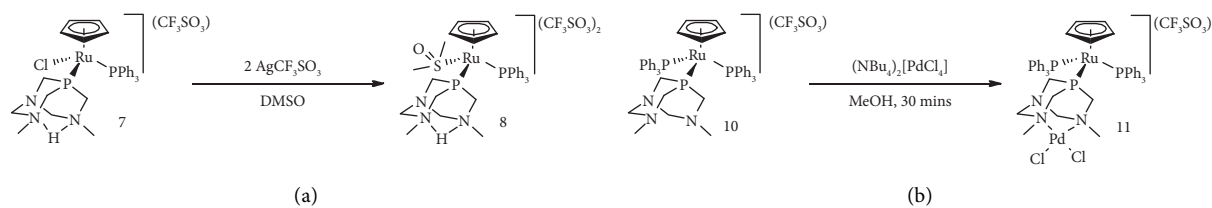
Scheme 1: Synthesis of **8** (a) and **11** (b).
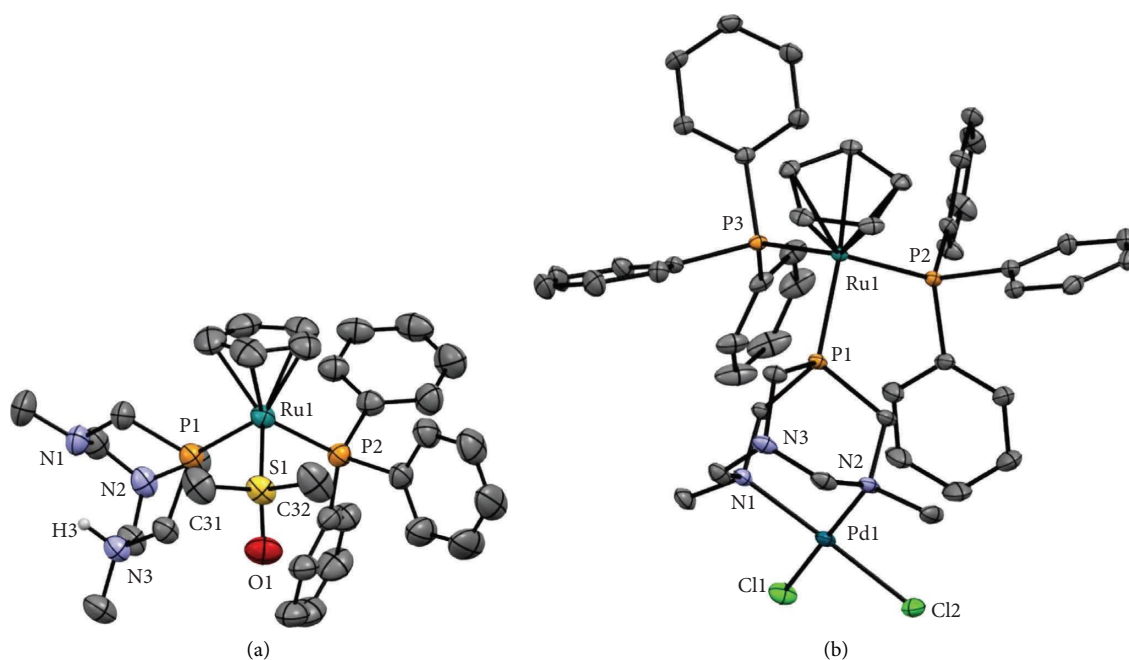
Figure 2: ORTEP view (50% probability) with atom numbering of the key atoms of the complex unit in the crystal structures of **8** (a) and **11** (b). Relevant bond lengths, plane, and torsion angles are given in Tables S2–S6 in SI. Anions, solvent molecules, and hydrogen atoms connected to the carbon atoms were omitted for clarity.

signals relative to the coordinated PPh$_3$ groups (39.93 ppm, *d*) and the {dmoPTA-PdCl$_2$} unit (−12.07 ppm, *t*) (Figures S17-S18) during 48 h. Nevertheless, a small set of signals corresponding to complex **8** becomes visible after 4 h (<7%), remaining constant up to 48 h. Therefore, only a marginal fraction of **11** undergoes solvolysis in DMSO. In DMSO-d$_6$/D$_2$O (1 : 1), the ^{31}P{^{1}H} NMR spectrum of this complex displays broad bands centred at +38.86 ppm assigned to the coordinated PPh$_3$ ligands, and different signals, some of them broad, for the {dmoPTA-PdCl$_2$} moiety (Figures S19 and S20). These sets of signals may only be explained by the presence of isomers of **11** in dissolution that might be the product of a rapid process involving dissociation and formation of the Pd–N bonds, as observed for previously reported similar complexes [26].

3.2.2. Cytotoxicity Studies. The cytotoxicity of free-PTA ligands (**1**–**3**) and ruthenium complexes (**4**–**11**) was evaluated using the colorimetric MTT assay against human breast cancer cells MDA-MB-231 and, for the most active compounds, also the MCF-7 cancer cells (Table 1). These cells were selected

considering their differences in terms of aggressiveness: the MDA-MB-231 cell line is highly aggressive, invasive, and hormone-independent (estrogen insensitive), while the MCF-7 cell line is noninvasive and hormone-dependent (estrogen sensitive) [46]. The cells were treated with concentrations of compounds in the range of 0.1–100 mM. None of the ligands **1**–**3** were found to be cytotoxic against the evaluated cancer cells (Table 1). In marked contrast, all ruthenium complexes, but **4**, display a notably much better activity (lower IC$_{50}$ value) than cisplatin which was used as the positive control. The results obtained suggest a general trend that was seen for other related ruthenium-cyclopentadienyl compounds: cationic complexes are more cytotoxic than neutral ones (compounds **4-5** vs. **6–10**) [47, 48]. In addition, and as previously observed, a PPh$_3$ ligand in the complex structure, but particularly in combination with methylated-PTA, improves cytotoxicity (Scheme 2) [23, 27, 49].

Moderate cytotoxicity is observed for complex **5**, whose structural difference with respect to **4** (noncytotoxic) is the presence of a PPh$_3$ ligand instead of one of the two PTA ligands. A 7-fold increase in cytotoxicity with respect to complex **5** is shown, when the PTA ligand is replaced by an

TABLE 1: Cytotoxicity studies.

Compounds					MDA-MB-231	MCF-7	HDF
Cisplatin [44, 45]	—	—	—	—	>100	38 ± 1.4	~100
1		PTA		0	>100	—	—
2		mPTA		+1	>100	—	—
3		dmPTA		+2	>100	—	—
Structure [Ru(Cp)$L^1L^2L^3$]	L^1	L^2	L^3	Charge			
4	Cl^-	PTA	PTA	0	>100	—	—
5	Cl^-	PPh$_3$	PTA	0	60 ± 19	—	—
6	Cl^-	PPh$_3$	mPTA	+1	8.3 ± 1.4	—	—
7	Cl^-	PPh$_3$	HdmoPTA	+1	2.5 ± 1.1	—	—
8	κS-DMSO	PPh$_3$	HdmoPTA	+2	15 ± 2.2	—	—
9	PPh$_3$	PPh$_3$	HdmoPTA	+2	0.86 ± 0.13	0.48 ± 0.07	1.23 ± 0.32
10	PPh$_3$	PPh$_3$	dmoPTA	+1	0.84 ± 0.09	0.40 ± 0.04	1.47 ± 0.40
11	PPh$_3$	PPh$_3$	dmoPTA-PdCl$_2$	+1	1.1 ± 0.2	0.73 ± 0.11	1.59 ± 0.45

The IC$_{50}$ values (μM) found after 24 h incubation of compounds **1–11** with MDA-MB-231 and of compounds **9**, **10**, and **11** with MCF-7 breast cancer cells and normal human fibroblasts (HDF). Values are the average of at least three experiments (±SD).
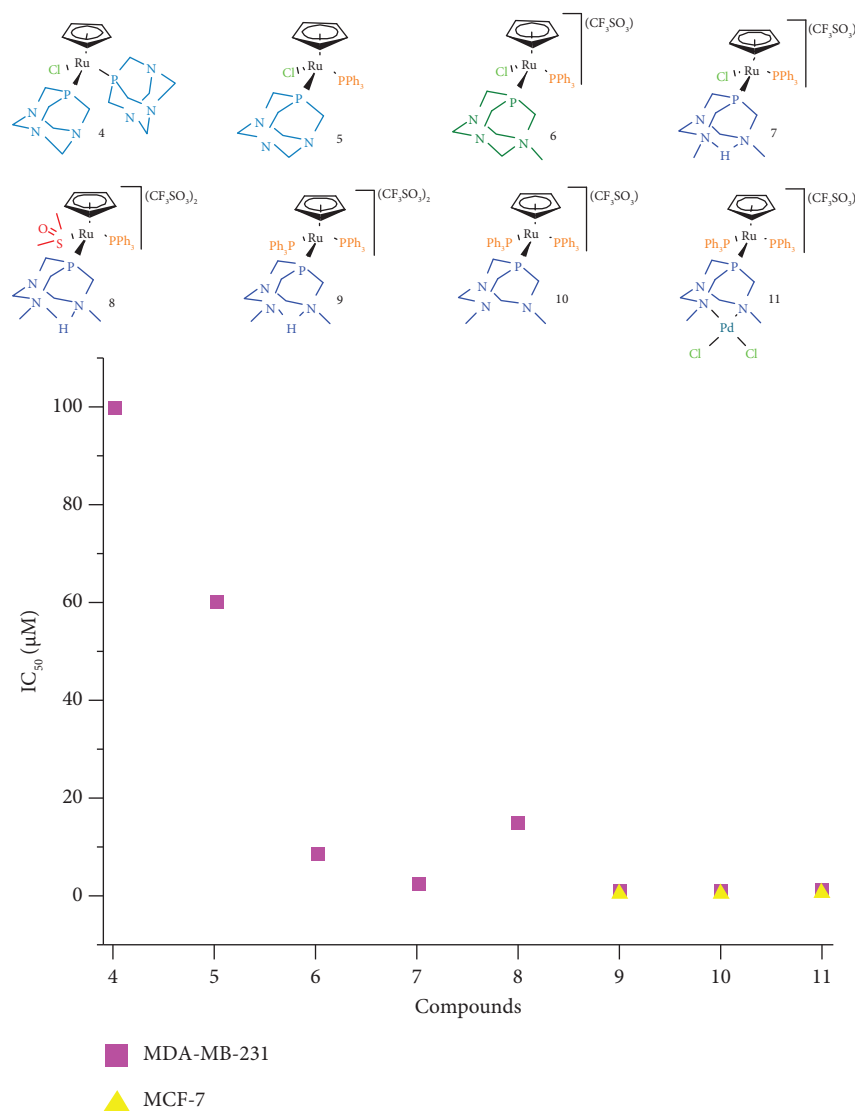
SCHEME 2: Representation of antiproliferative activity tendency of compounds **4–11**.

mPTA ligand, as in cationic complex **6**. A 4-fold increase in antiproliferative activity can be observed with respect to complex **6**, when HdmoPTA is replaced by an mPTA ligand in the structure of the complex as it happens in **7**. Observing the structural changes in which the antiproliferative activity has increased, complexes **9** and **10** were the most active. Their structures present a combination of PPh$_3$ and dimethylated PTA, in place of Cl$^-$ and PTA. However, a marked decrease in antiproliferative activity is observed when there is DMSO in place of Cl$^-$, as in complex **8**, although the antiproliferative activity is still significant. Nevertheless, and interestingly, the coordination of one {PdCl$_2$} moiety to the CH$_3$N$_{dmoPTA}$ nitrogen atoms, which gives rise to Ru-Pd heterometallic complex **11**, provides an activity quite similar to those of **9** and **10** [24, 27].

Complexes **9–11**, with the best antiproliferative activity in hormone-independent MDA-MB-231 cells, were further evaluated against the MCF-7 cells, showing even better cytotoxicity activity against this hormone-dependent cancer cell line: IC$_{50}$ values were ~2-fold lower and very markedly surpassed cisplatin by more than one order of magnitude. In addition, complexes **9–11** were tested against normal human dermal fibroblasts (HDF) to evaluate the selectivity for cancer cells. Compared to fibroblasts, complexes **9**, **10**, and **11** are 1.5-fold and ~2-3-fold less cytotoxic than for MDA-MB-231 cells and MCF-7 cells, respectively. These results are important although not clinically relevant. While further studies are needed, the overall results show that complexes **9–11** seem prospective candidates as metallodrugs for breast cancer showing remarkable activity (in the submicromolar range) against the aggressive, highly metastatic, and cisplatin-resistant MDA-MB-231 line, a model of triple-negative breast cancer, as well as for hormone-dependent MCF-7 cancer cells, largely surpassing the activity of cisplatin by ~50 fold.

3.2.3. Cell Death Measurement Using Flow Cytometry: The Annexin V/PI Assay.

To determine the cell death mechanism caused by **9–11**, the annexin V/propidium iodide (AV/PI) cytometry-based assay was carried out in the MDA-MB-231 cells after 24 h incubation with complexes at their IC$_{50}$ concentrations. Results showed that all compounds mostly induce apoptosis with less than 10% necrosis and that the cells appear at late apoptosis (Figure 3). Induced cell death by apoptosis, a controlled and programmed mechanism of disposal of damaged cells and their content, is a desirable feature for any drug and reinforces the interest of compounds **9–11** as prospective therapeutics.

3.2.4. Complex Cell Uptake and Subcellular Distribution.

The intracellular distribution of complexes **9–11** in MDA-MB-231 cells was investigated after 6 h and 24 h incubations at their respective IC$_{50}$ values. Cytosol, membranes, nucleus, and cytoskeletal fractions were extracted using a commercial kit, and the ruthenium content in each fraction was quantified by ICP-MS. Results are summarized in Figure 4.

The results clearly show that all three complexes are mainly accumulated at cell membranes (>86% for 6 h
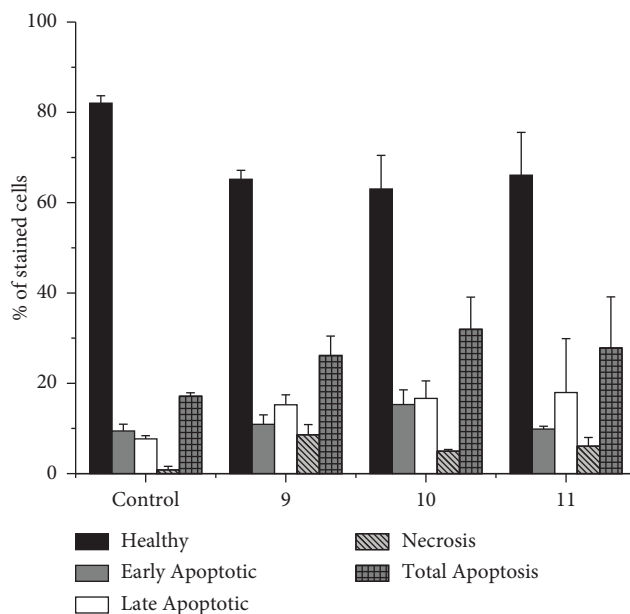

Figure 3: Ruthenium-based compounds potentiate apoptotic cell death in the MDA-MB-231 breast cancer cell line. Apoptotic cell death was analysed by the annexin V fluorescein isothiocyanate (AV-FITC) and propidium iodide (PI) assay in MDA-MB-231 cells, after incubation with IC$_{50}$ concentrations for 24 h graphical representation of the annexin V/PI dot plots of flow cytometry data analysed using Flowing software for control and compounds **9–11**.

incubation, >90% for 24 h incubation, Figure 4), while ca. 10% or less in the nucleus and marginally in cytosol and cytoskeletal. These results agree with previously published related works on ruthenium-cyclopentadienyl-phosphane-based compounds [44, 50]. No relevant differences in the ruthenium uptake between compounds are observed, possibly due to the very high structural resemblance at the Ru(II) coordination sphere. Despite complex **11** being constituted by Ru and Pd, the observed amount of this last metal in the membranes was only residual, and no evidence of its presence in other organelles of cells was found.

3.2.5. Binding Interaction with Human Serum Albumin by Steady-State and Time-Resolved Fluorescence Spectroscopy.

A desirable feature, included in the FDA requirements, for any metallodrug aimed at therapeutic application, is its ability to be transported and distributed within the system where required, at the target sites. This aspect was accessed for complexes **9–11**: the possibility of their transport in blood was modelled by the interaction with human serum albumin, the most abundant protein in blood plasma and the major transport vehicle for endo/exogenous compounds in the human system.

Fluorescence spectroscopy was used to assess the interaction between compounds and HSA [50, 51]. HSA exhibits intrinsic fluorescence due to the presence of its phenylalanine, tyrosine, and tryptophan (Trp) residues, of which single Trp at position 214 is the dominant fluorophore [51–55]. Trp214 is located in protein subdomain IIA, near Sudlow's drug binding site I, and it is very sensitive to
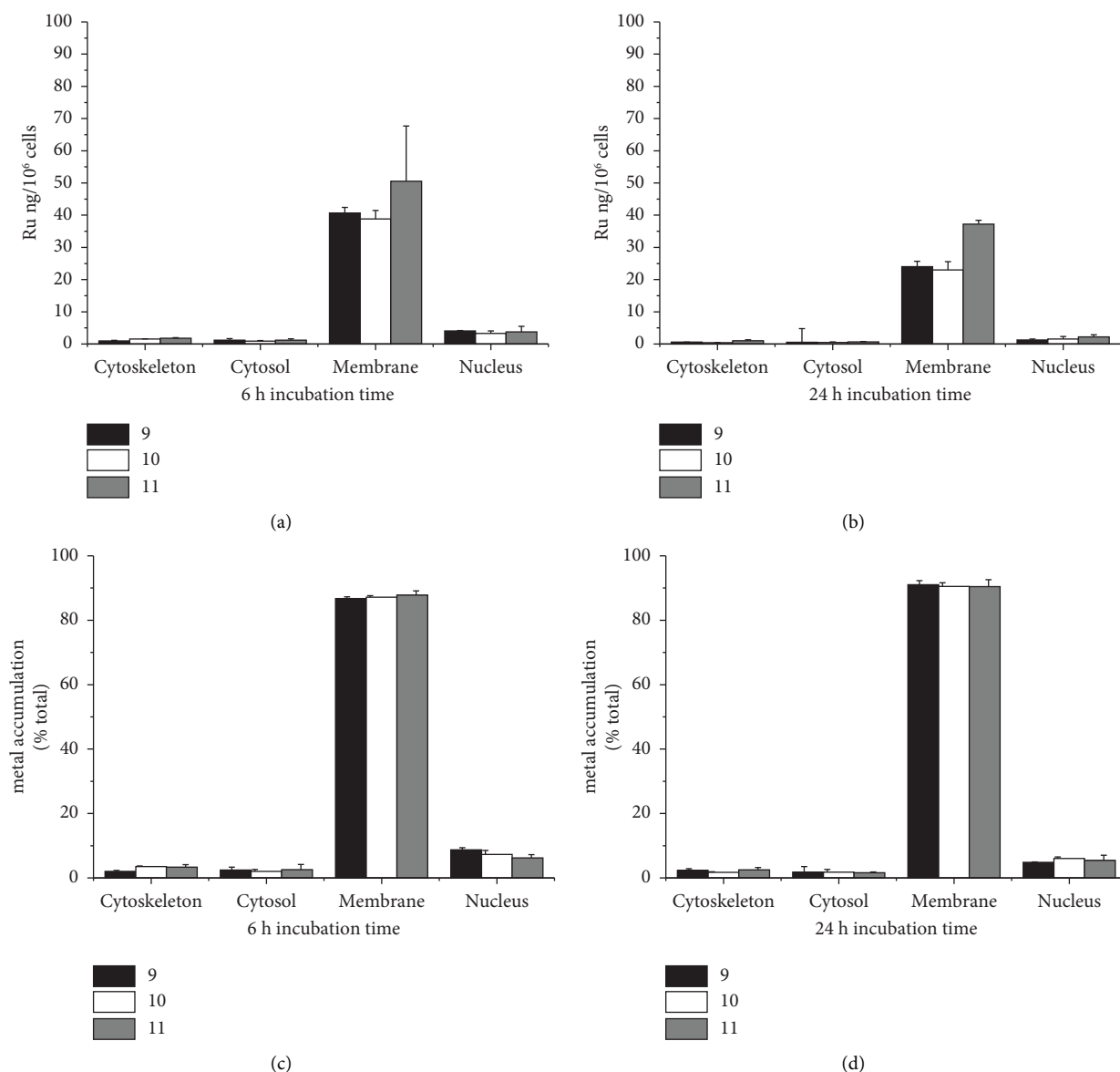
(a)

(b)

(c)

(d)

Figure 4: Cellular Ru distribution of **9–11** in MDA-MB-23 cells at two different time points: the amount of Ru determined by ICP-MS for each subcellular fraction (normalized, 10^6 cells) at 6 h (a) and 24 h (b); Ru accumulation (relative %) profile at 6 h (c) and 24 h (d).

changes in its microenvironment, which can occur following drug binding in its vicinity or due to structural alterations of protein. Thus, it can also probe interactions at drug-binding site II [56–58]. In this work, we used the intrinsic fluorescence of HSA and selectively monitored the fluorescence emission by Trp214 for constant protein concentration, in the presence of increasing concentrations of the complex [38, 50, 55, 59].

(1) Steady-State and Time-Resolved Fluorescence Emission. Emission spectra of HSA-Trp214 were acquired in the presence of increasing concentrations of the compounds after an incubation period of 24 h. As can be observed in Figure 5, in the absence of the complex, the maximum emission intensity for Trp214 occurs at 334 nm (red line in Figure 5), in agreement with previous reports [51, 56, 58],

and denoting that the indole side chain of Trp214 is not fully exposed to the aqueous solvent, where the maximum emission of Trp would occur at ca. 350 nm [53, 61, 62]. Ru-compounds **9** and **10** do not induce any spectral shift, unlike complex **11**, which causes a small blueshift of the emission by Trp214 (Figure S22). Nonetheless, all complexes caused a marked and concentration-dependent decrease in the Trp214 fluorescence intensity.

The emission intensity of Trp214 after 24 h, at a 20 μM concentration of **9**, **10**, and **11** (corresponding to a 1 : 4 HSA:compound ratio), reached approximately 60%, 75%, and 40%, respectively, of the value measured in the absence of compound (Figure 5, inset). This clear quenching of Trp214 fluorescence indicates that there is a strong interaction between the protein and the three complexes.
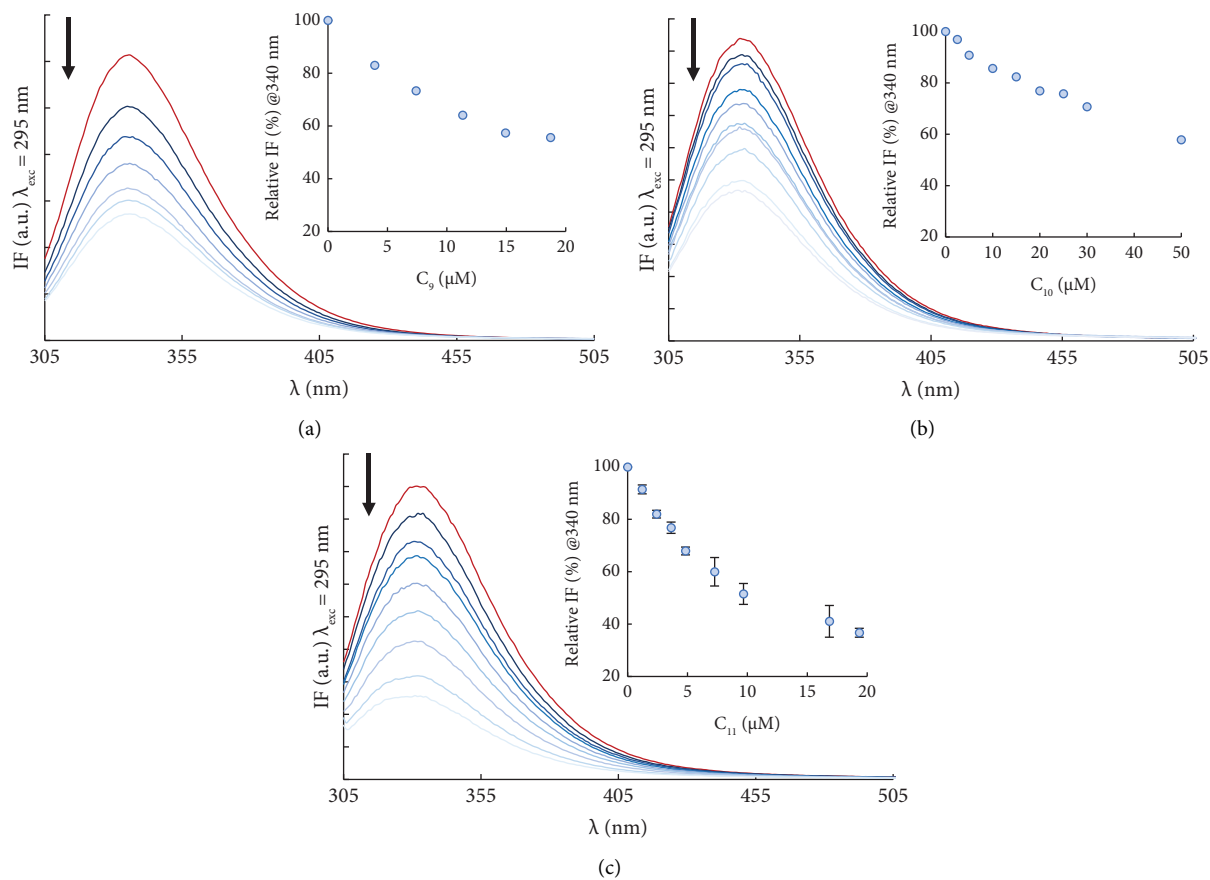
(a)

(b)

(c)

Figure 5: The complexes are effective quenchers of the steady-state fluorescence emission of HSA-Trp214: emission spectra of HSA in the absence (red, top line) and in the presence (blue) of increasing concentrations of **9** (a), **10** (b), and **11** (c) after an incubation of 24 h at 37°C (arrows indicate the change with increasing complex concentration). Insets: the relative fluorescence intensity (%) at $\lambda_{em} = 340$ nm with increasing complex concentrations, corrected for inner filter effects [40, 60] (conditions: PBS pH 7.4/2% (v/v) DMSO; $C_{HSA} = 3.7 \mu$M for (a) and 5.0μM for (b, c); $\lambda_{exc} = 295$ nm; spectra recorded at 25.0 ± 0.1°C).

The increase in absorbance for the longer wavelengths in the absorption spectra for concentrations higher than 10μM of **11** is consistent with the formation of an aggregate (Figure S21) [62], which only occurs in the presence of HSA. Thus, high concentrations of **11** may induce HSA aggregation to some extent, which would also explain the previously noted small blueshift of the emission spectra induced by this complex (Figure S22). The global environment of the Trp214 residue would become less polar in the aggregates as it is even more protected from the aqueous environment, leading to the blueshift in emission. In addition, the formation of protein aggregates would also lead to increased light scattering, which is evidenced by the rise in the tail of the absorption spectra of the sample (i.e., an increase in absorbance in a spectral region where none of the species present absorbs light). Nevertheless, it is important to point out that this phenomenon should be of little relevance to the biological effect of the complex because the plasma concentration of HSA is much higher than that used in this study and because the IC_{50} values of **11** are clearly below 10μM.

To differentiate multiple binding modes near Trp214 and uncover the quenching mechanism underlying the interaction between HSA and studied complexes, time-resolved fluorescence measurements were carried out. The single-decay analysis of the time-resolved fluorescence of Trp214 measured at different concentrations for each compound revealed a typical triple exponential behaviour [51, 52], e.g., for HSA-Trp214 (Figure S23). For the protein in the absence of the compound, the amplitudes were $\alpha_1 = 0.34 \pm 0.01$, $\alpha_2 = 0.41 \pm 0.01$, and $\alpha_3 = 0.25 \pm 0.01$; the lifetime components were $\tau_1 = (1.03 \pm 0.13)$ ns, $\tau_2 = (3.95 \pm 0.13)$ ns, and $\tau_3 = (7.31 \pm 0.01)$ ns; and the amplitude-weighted mean fluorescence lifetime, $\bar{\tau}$, was (3.80 ± 0.15) ns, all in agreement with previous reports [51, 52]. With the calculated amplitude-weighted mean fluorescence lifetime values, it is possible to represent a fluorescence lifetime Stern–Volmer plot (Figure 6).

Figure 6 shows that the presence of **9** and **10** does not affect the mean fluorescence lifetime of HSA-Trp214 regardless of the concentration used. This fact indicates that these complexes quench the steady-state fluorescence of HSA without affecting its fluorescence lifetime. This result points to the formation of a nonfluorescent ground state complex through the binding of **9** and **10** to the protein near the Trp214 residue.
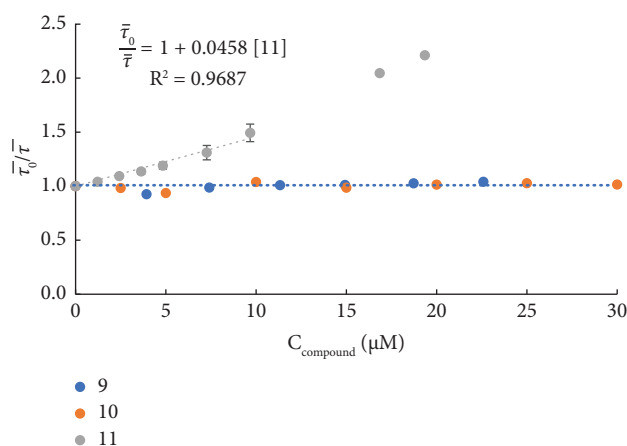
Figure 6: Compound **11**, but not **9** or **10**, affects the amplitude-weighted mean fluorescence lifetime of HSA-Trp214 for a Stern–Volmer plot built from the fluorescence lifetimes of HSA Trp214 in the presence of increasing concentrations of each compound: ratio of the amplitude-weighted mean fluorescence lifetime (see equation (2) in 2.4.6 Interaction with Human Serum Albumin) in the absence ($\bar{\tau}_0$) and presence ($\bar{\tau}$) of the complex (conditions: PBS pH 7.42% (v/v) DMSO; C_{HSA} = 3.7 μM for **9** and 5.0 μM for **10** and **11** μM; λ_{em} = 350 nm; the samples were incubated for 24 h at 37°C; the fluorescence intensity decays were recorded at 25.0 ± 0.1°C).

In contrast, the amplitude-weighted mean fluorescence lifetime of Trp214 decreased in the presence of **11**, which suggests that dynamic quenching might be occurring. Typical Stern–Volmer constants are in the order of 10 mM–100 mM for dynamic quenching resulting from random collisions between the compound and the indole sidechain of Trp214; however, for the concentration range here used, there could be no appreciable collisional quenching. Therefore, the observed behaviour should mean that fluorescence lifetime is due to a stronger and more specific interaction related to a binding process. As both amplitude-weighted mean fluorescence lifetimes decrease to a larger extent in the steady-state fluorescence intensity, the presence of two independent binding sites should be considered: one of them in closer proximity to Trp214 than the other. However, more complex situations cannot be completely ruled out, such as two binding modes in the same binding site or two binding sites, both close to Trp214.

(2) Determination of the Compound-HSA-Binding Constants. The first approach to estimate the complex-HSA-binding constants based on fluorescence quenching is usually the inspection of the Stern–Volmer plots. No variation in the amplitude-weighted mean fluorescence lifetime was detected for compounds **9** and **10**. However, this was not the case for the steady-state fluorescence intensity-based Stern–Volmer plots which are shown in Figure 7.

Considering the absence of the effect on the fluorescence lifetimes for **9** and **10**, the slope of the Stern–Volmer plots in Figures 7(a) and 7(b) can be safely interpreted as a static quenching constant. In turn, in these two specific situations, the static quenching constant for Trp214 by each compound can be taken as the binding constant (K_B) for the formation of a ground state 1:1 nonfluorescent complex between HSA and the compound (equation (4)), according to the equilibrium:

$$\{HSA\}_{(aq)} + \{compound\}_{(aq)} \rightleftarrows \{HSA-compound\}_{(aq)}, \quad (3)$$
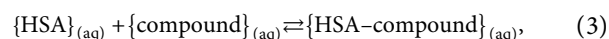
$$\frac{IF_0}{IF} = 1 + K_B C_{compound}, \quad (4)$$

where IF_0 and IF are, respectively, the fluorescence intensity of Trp214 of HSA in the absence and presence of the compound. The determined binding constant for **9** of $(4.59 \pm 0.21) \times 10^4 \cdot M^{-1}$ and of $(1.43 \pm 0.05) \times 10^4 \cdot M^{-1}$ for **10** correspond to log K_B values of (4.66 ± 0.04) for **9** and (4.16 ± 0.03) for **10**, respectively.

From a linear fit to the amplitude-weighted mean fluorescence lifetime of the Stern–Volmer plot for HSA-Trp214 quenching by **11** (Figure 6), it is possible to estimate conditional binding constant K'_B of $(4.58 \pm 0.33) \times 10^4 \cdot M^{-1}$. The two quenching processes, affecting the steady-state fluorescence intensity alone or together with the fluorescence lifetime, strongly suggest two binding modes as previously noted. Therefore, the following equation was fitted to the variation of the steady-state fluorescence intensity of Trp214 with an increasing concentration of **11** (Figure 7(c)):

$$\frac{IF_0}{IF} \approx 1 + (K_B + K'_B)C_{11} + (K_B K'_B)(C_{11})^2, \quad (5)$$

where K'_B was fixed to $(4.58 \pm 0.33) \times 10^4 \ M^{-1}$. A K_B of $(3.70 \pm 0.33) \times 10^4 \ M^{-1}$ was retrieved, corresponding to a log K_B of (4.57 ± 0.07). Moreover, as previously stated, K'_B can be considered an additional binding constant for the equilibrium between **11** and HSA, being log K'_B of (4.66 ± 0.07). Interestingly, both K_B and K'_B are in the same order of magnitude as all other binding constants determined. Note that concentrations of **11** above 10 μM were not considered for the estimation of either K_B or K'_B (Figures 6 and 7(c)), due to the possible aggregation of HSA, which was reported in the previous section.

$$\frac{IF_0}{IF} = 1 + 0.0459 \, [9]$$

$$R^2 = 0.9854$$

(a)

$$\frac{IF_0}{IF} = 1 + 0.0143 \, [10]$$

$$R^2 = 0.9913$$

(b)

$$\frac{IF_0}{IF} = 1 + 0.0827 \, [11] + 0.0017 \, [11]^2$$
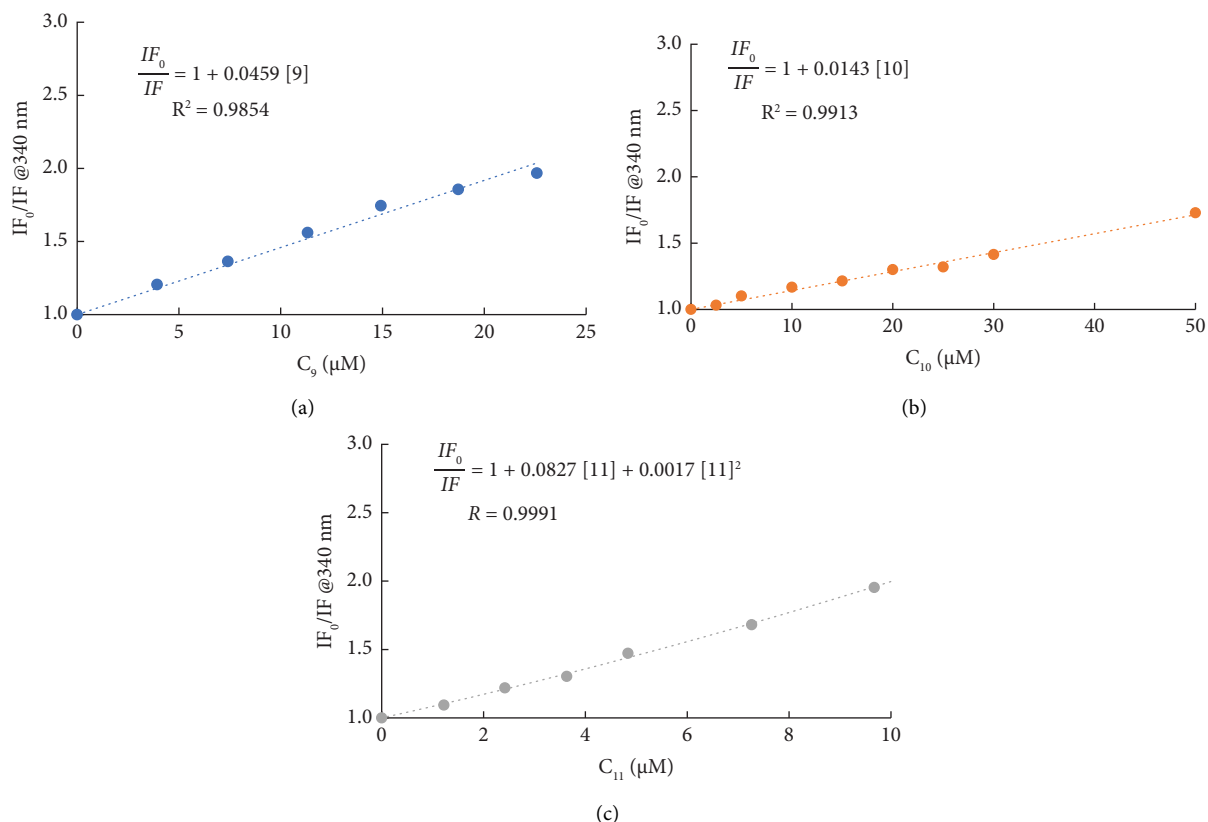
$$R = 0.9991$$

(c)

FIGURE 7: HSA-Trp214 steady-state fluorescence Stern–Volmer plots for quenching by the compounds. Variation in the fluorescence intensity of Trp214 at 340 nm obtained from steady-state measurements (corrected for inner filter and self-absorption effects) in the absence (IF_0) and presence (IF) of compounds **9** (a), **10** (b), and **11** (c) (conditions: PBS pH 7.4/2% (v/v) DMSO; $C_{HSA} = 3.7 \, \mu M$ for **9** and 5.0 μM for **10** and **11**, kept constant; $\lambda_{exc} = 295$ nm, $\lambda_{em} = 340$ nm; the samples were incubated for 24 h at 37°C; spectra were recorded at 25.0 ± 0.1°C).

TABLE 2: Parameters determined for the binding of **9**, **10**, and **11** with HSA.

Compound	Type of quenching	Equation used	$K_B \times 10^4$ (M^{-1})	$K_B' \times 10^4$ (M^{-1})	Log K_B	Log K_B'
9	Static	3	4.59 ± 0.21	—	4.66 ± 0.04	—
10	Static	3	1.43 ± 0.05	—	4.16 ± 0.03	—
11	"Dynamic" and static	4	3.70 ± 0.33	4.58 ± 0.33	4.57 ± 0.07	4.66 ± 0.07

Conditions: PBS pH 7.4/2% (v/v) DMSO; $C_{HSA} = 3.7 \, \mu M$ for **9** and 5.0 μM for **10** and **11** μM, kept constant; the samples were incubated for 24 h at 37°C.

Table 2 presents the summary of all the binding constants determined for the interaction of HSA with **9**, **10**, and **11**.

The K_B values obtained for the interaction of HSA with each compound are very similar. Also, the strong interaction of ruthenium [51] and copper complexes [58, 63] with HSA determined in previous works is comparable with the values of binding constants obtained herein for all three compounds. Interestingly, heterodimetallic complex **11** is the one with the strongest interaction with HSA, due to the two modes of interaction that are relatively efficient. Monometallic parent complexes **9** and finally **10** show a similar interaction with HSA, which is smaller than that observed for **11**. Log K_B obtained for complexes **9**–**11** are of the same order of magnitude as the one found for the Ru(III) complex KP1019, known to be transported in blood by serum albumin and to bind the protein reversibly [57]. Our results

thus suggest that all three compounds, **9**, **10** and **11**, can be efficiently transported by albumin in blood plasma.

4. Conclusions

Complex [RuCp(DMSO-κS)(HdmoPTA)(PPh$_3$)](CF$_3$SO$_3$)$_2$ (**8**) and heterodimetallic [RuCp(PPh$_3$)$_2$(dmoPTA-1κP-2$\kappa^2 N,N'$-PdCl$_2$)](CF$_3$SO$_3$) (**11**) were characterized by elemental analysis, IR, and multinuclear NMR, and their crystal structures were determined by single-crystal X-ray diffraction. Also, the stability of these complexes in DMSO and DMSO/D$_2$O was performed, resulting in **8** formed in low proportion (<7%) when **11** is dissolved in pure DMSO.

Not only the cytotoxic activities of all the complexes (**4**–**11**) but also those of ligands PTA (**1**), mPTA (**2**), and dmPTA (**3**) were evaluated against the MDA-MB-231 and MCF-7 breast cancer cells using the MTT assay. The most

active complexes against both breast cancer cells were **9**, **10**, and **11**, showing IC_{50} values in the micromolar range, suggesting that the highest cytotoxicity is achieved when two PPh_3 ligands and one dmoPTA ligand were combined around the metal in the {CpRu} moiety. These complexes were also tested against normal human dermal fibroblasts (HDFs) to evaluate the selectivity for cancer cells, being 1.5-fold and ~2-3-fold less cytotoxic than for MDA-MB-231 cells and MCF-7 cells, respectively. Studies by flow cytometry showed that these three complexes induce mostly apoptosis in combination with a small percentage of necrosis (<10%) on MDA-MB-231 cells, which is very positive for their possible use as a drug. Cell distribution studies of the three complexes showed that Ru is mostly retained in the cell membrane (ca. 90%) and a reduced quantity in the cell nucleus (<10%) of MDA-MB-231 cells. It is important to stress that Pd metal was not found in a significant quantity in cells when **11** was evaluated. Experiments to determine the binding interaction with human serum albumin were carried out, concluding that the presence or absence of an H-bridge between CH_3N_{dmoPTA} determines the interaction mechanism with the carrier blood protein. Also, an interesting conclusion is that Ru-Pd heterobimetallic complex **11** interacts with HSA to a higher extent and by a different mechanism with respect to monometallic complexes. The obtained results show how the combination of ligands around Ru determines the antiproliferative activity of this family of complexes, but the fact that Ru is located mainly in the cell membrane suggests that these ligands should affect how the cell membrane works, being the factor that induces their cytotoxic activity. The fact that Pd is not located in the cell also suggests that complex **11** decomposes, releasing the Pd atom before interacting with the cells, but the fact that this complex interacts with HSA by a different mechanism than **9** and **10** also suggests that this extra metal can determine how the complex arrives to the cell, being this also an important role related to the antiproliferative activity. Additional experiments are in progress to determine these suspicions. Overall, complexes **9** and **10** emerge from this work as interesting and highly promising to pursue to further studies as prospective ruthenium metallodrugs.

Data Availability

Crystallographic data for the structures reported in this manuscript have been deposited with the Cambridge Crystallographic Data Centre under the CCDC codes 2263437 and 2261422. These data can be obtained free of charge via http://www.ccdc.cam.ac.uk/data_request/cif, or by emailing data_request@ccdc.cam.ac.uk, or by contacting the Cambridge Crystallographic Data Centre, 12 Union Road, Cambridge CB2 1EZ, UK; fax: +44 1223 336033.

Conflicts of Interest

The authors declare no conflicts of interest.

Acknowledgments

Supplementary Materials

Supplementary Materials contains experimental procedures, NMR data, X-ray crystallographic data for **8** and **11**, and antiproliferative and biological studies: stability tests in $DMSO-d_6$ and $DMSO-d_6/D_2O$ under air atmosphere; cell lines and culture conditions; compound cytotoxicity evaluated using the MTT assay; cell death measurement using flow cytometry: the annexin V/PI assay; complex uptake and distribution by ICP-MS; binding interaction with human serum albumin by steady-state and time-resolved fluorescence emission. Also, separate check cif files (PDF) for crystal structures of **8** and **11** were provided. (*Supplementary Materials*)

References

[1] B. Rosenberg, L. Van Camp, and T. Krigas, "Inhibition of cell division in *Escherichia coli* by electrolysis products from a platinum electrode," *Nature*, vol. 205, no. 4972, pp. 698-699, 1965.

[2] B. Rosenberg, L. VanCamp, J. E. Trosko, and V. H. Mansour, "Platinum compounds: a new class of potent antitumour agents," *Nature*, vol. 222, no. 5191, pp. 385-386, 1969.

[3] K. D. Mjos and C. Orvig, "Metallodrugs in medicinal inorganic chemistry," *Chemistry Review*, vol. 114, no. 8, pp. 4540–4563, 2014.

[4] R. F. Ozols, B. N. Bundy, B. E. Greer et al., "Phase III trial of carboplatin and paclitaxel compared with cisplatin and paclitaxel in patients with optimally resected stage III ovarian cancer: a Gynecologic Oncology Group study," *Journal of Clinical Oncology*, vol. 21, no. 17, pp. 3194–3200, 2003.

[5] Y. Bécouarn, M. Ychou, M. Ducreux et al., "Phase II trial of oxaliplatin as first-line chemotherapy in metastatic colorectal cancer patients. Digestive Group of French Federation of Cancer Centers," *Journal of Clinical Oncology*, vol. 16, no. 8, pp. 2739–2744, 1998.

[6] C. A. Rabik and M. E. Dolan, "Molecular mechanisms of resistance and toxicity associated with platinating agents," *Cancer Treatment Reviews*, vol. 33, no. 1, pp. 9–23, 2007.

[7] E. Gao, C. Liu, M. Zhu, H. Lin, Q. Wu, and L. Liu, "Current development of Pd(II) complexes as potential antitumor agents," *Anti-Cancer Agents in Medicinal Chemistry*, vol. 9, no. 3, pp. 356–368, 2009.

[8] T. J. Carneiro, A. S. Martins, M. P. M. Marques, and A. M. Gil, "Metabolic aspects of palladium(II) potential anti-cancer drugs," *Frontiers Oncology*, vol. 10, Article ID 590970, 2020.

[9] J. Coleman, D. Sjoberg, Q. Demac et al., "MP46-04 results of the PCM-204 phase 2B trial of partial-gland ablation for men with intermediate-risk prostate cancer with padeliporfin (WST11 or tookad) vascular-targeted photodynamic therapy," *The Journal of Urology*, vol. 206, no. 3, 2021.

[10] A. Levina, A. Mitra, and P. A. Lay, "Recent developments in ruthenium anticancer drugs," *Metallomics*, vol. 1, no. 6, pp. 458–470, 2009.

[11] G. Sava, K. Clerici, I. Capozzi et al., "Reduction of lung metastasis by ImH[trans-RuCl4(DMSO)Im]: mechanism of the selective action investigated on mouse tumors," *Anti-Cancer Drugs*, vol. 10, no. 1, pp. 129–138, 1999.

[12] E. Alessio and L. Messori, "NAMI-A and KP1019/1339, two iconic ruthenium anticancer drug candidates face-to-face: a case story in medicinal inorganic chemistry," *Molecules*, vol. 24, no. 10, p. 1995, 2019.

[13] S. Monro, K. L. Colón, H. Yin et al., "Transition metal complexes and photodynamic therapy from a tumor-centered approach: challenges, opportunities, and highlights from the development of TLD1433," *Chemistry Review*, vol. 119, no. 2, pp. 797–828, 2019.

[14] Intravesical Photodynamic Therapy (PDT), "BCG refractory/ intolerant non-muscle invasive bladder cancer (NMIBC) patients-full text view-ClinicalTrials.gov," 2023, https:// clinicaltrials.gov/ct2/show/NCT03945162?term=tld1433&draw= 2&rank=2.

[15] C. S. Allardyce, P. J. Dyson, D. J. Ellis, and S. L. Heath, "[Ru(η6-p-cymene)Cl2(pta)] (pta = 1,3,5-triaza-7-phospha-tricyclo- [3.3.1.1]decane): a water soluble compound that exhibits pH dependent DNA binding providing selectivity for diseased cells," *Chemical Communications*, no. 15, pp. 1396-1397, 2001.

[16] B. S. Murray, M. V. Babak, C. G. Hartinger, and P. J. Dyson, "The development of RAPTA compounds for the treatment of tumors," *Coordination Chemistry Reviews*, vol. 306, pp. 86–114, 2016.

[17] M. Rausch, P. J. Dyson, and P. Nowak-Sliwinska, "Recent considerations in the application of RAPTA-C for cancer treatment and perspectives for its combination with immunotherapies," *Advanced Therapeutics*, vol. 2, no. 9, Article ID 1900042, 2019.

[18] D. J. Daigle, A. B. Pepperman, and S. L. Vail, "Synthesis of a monophosphorus analog of hexamethylenetetramine," *Journal of Heterocyclic Chemistry*, vol. 11, no. 3, pp. 407-408, 1974.

[19] A. K. Renfrew, A. D. Phillips, A. E. Egger et al., "Influence of structural variation on the anticancer activity of RAPTA-type complexes: ptn versus pta," *Organometallics*, vol. 28, no. 4, pp. 1165–1172, 2009.

[20] A. Wołoszyn, C. Pettinari, R. Pettinari et al., "Ru(II)-(PTA) and -mPTA complexes with N2-donor ligands bipyridyl and phenanthroline and their antiproliferative activities on human multiple myeloma cell lines," *Dalton Transactions*, vol. 46, no. 30, pp. 10073–10081, 2017.

[21] B. Kar, N. Roy, and P. Paira, "Ru(II)arene(NN bpy/phen)-based RAPTA complexes for in vitro anti-tumour activity in human glioblastoma cancer cell lines and in vivo toxicity studies in a zebrafish model," *RSC Advances*, vol. 12, no. 29, pp. 18911–18922, 2022.

[22] V. Ferretti, M. Fogagnolo, A. Marchi, L. Marvelli, F. Sforza, and P. Bergamini, "Acetylcholine-like and trimethylglycine-like PTA (1,3,5-triaza-7-phosphaadamantane) derivatives for the development of innovative Ru-and Pt-based therapeutic agents," *Inorganic Chemistry*, vol. 53, no. 10, pp. 4881–4890, 2014.

[23] A. Mena-Cruz, P. Lorenzo-Luis, A. Romerosa, M. Saoud, and M. Serrano-Ruiz, "Synthesis of the water soluble ligands dmPTA and dmoPTA and the complex [RuClCp(HdmoP-TA)(PPh3)](OSO2CF3) (dmPTA = N,N′-dimethyl-1,3,5-tri-aza-7-phosphaadamantane, dmoPTA = 3,7-dimethyl-1,3,7-triaza-5-phosphabicyclo[3.3.1]nonane, HdmoPTA = 3,7-H-3,7-dimethyl-1,3,7-triaza-5-phosphabicyclo[3.3.1]nonane)," *Inorganic Chemistry*, vol. 46, no. 15, pp. 6120–6128, 2007.

[24] Z. Mendoza, P. Lorenzo-Luis, F. Scalambra, J. M. Padrón, and A. Romerosa, "One step up in antiproliferative activity: the Ru-Zn complex [RuCp(PPh3)2-μ-dmoPTA-1κP:2κ2N,N′-ZnCl2](CF3SO3)," *European Journal of Inorganic Chemistry*, vol. 2018, no. 43, pp. 4684–4688, 2018.

[25] A. Mena-Cruz, P. Lorenzo-Luis, A. Romerosa, and M. Serrano-Ruiz, "Water-soluble 3,7-dimethyl-1,3,7-triaza-5-phosphabicyclo[3.3.1]nonane (dmoPTA) as a polydentate ligand: synthesis of [RuClCp(PPh3)-μ-dmoPTA-1κP: 2κ2N,N′-Co(acac-κ2O, O′)2]·H2O," *Inorganic Chemistry*, vol. 47, no. 7, pp. 2246–2248, 2008.

[26] A. Mena-Cruz, P. Lorenzo-Luis, V. Passarelli, A. Romerosa, and M. Serrano-Ruiz, "Comparative study of [RuClCp(Hd-moPTA-κP)(PPh3)] [CF 3SO3] and the heterobimetallic complexes [RuClCp(PPh 3)-μ-dmoPTA-1κP:2κ2N,N′-M(acac- κ2O,O′)2] (M = Co, Ni, Zn; DmoPTA = 3,7-di-methyl-1,3,7-triaza-5-phosphabicyclo[3.3.1]nonane)," *Dalton Transactions*, vol. 40, no. 13, pp. 3237–3244, 2011.

[27] Z. Mendoza, P. Lorenzo-Luis, M. Serrano-Ruiz et al., "Synthesis and antiproliferative activity of [RuCp(PPh3) 2(HdmoPTA)](OSO2CF3)2 (HdmoPTA = 3,7-H-3,7-Di-methyl-1,3,7-triaza-5-phosphabicyclo[3.3.1]nonane)," *Inorganic Chemistry*, vol. 55, no. 16, pp. 7820–7822, 2016.

[28] Z. Mendoza, P. Lorenzo-Luis, F. Scalambra, J. M. Padrón, and A. Romerosa, "Enhancement of the antiproliferative activity of [RuCp(PPh3)2(dmoPTA-1κP)]+: via its coordination to one {CoCl2} unit: synthesis, crystal structure and properties of [RuCp(PPh3)2-μ-dmoPTA-1κP:2κ2 N, N′-CoCl2](OTf)· 0.25H2O," *Dalton Transactions*, vol. 46, no. 25, pp. 8009–8012, 2017.

[29] N. Kordestani, E. Abas, L. Grasa, A. Alguacil, F. Scalambra, and A. Romerosa, "The significant influence of a second metal on the antiproliferative properties of the complex [Ru(η6−C10H14)(Cl2)(dmoPTA)]," *Chemistry*, vol. 28, no. 3, Article ID e202103048, 2022.

[30] A. Romerosa, T. Campos-Malpartida, C. Lidrissi et al., "Synthesis, characterization, and dna binding of new water-soluble cyclopentadienyl ruthenium(ii) complexes incorporating phosphines," *Inorganic Chemistry*, vol. 45, no. 3, pp. 1289–1298, 2006.

[31] D. N. Akbayeva, L. Gonsalvi, W. Oberhauser et al., "Synthesis, catalytic properties and biological activity of new water soluble ruthenium cyclopentadienyl PTA complexes [(C5R5) RuCl(PTA)2] (R = H, Me; PTA = 1,3,5-triaza-7-phosphaa-damantane)," *Chemical Communications*, no. 2, pp. 264-265, 2003.

[32] G. M. Sheldrick, "Crystal structure refinement with SHELXL," *Acta Crystallographica, Section C: Structural Chemistry*, vol. 71, no. 1, pp. 3–8, 2015.

[33] G. M. Sheldrick, "*SHELXT*– Integrated space-group and crystal-structure determination," *Acta Crystallographica*

Section A Foundations and Advances, vol. 71, no. 1, pp. 3–8, 2015.

[34] O. V. Dolomanov, L. J. Bourhis, R. J. Gildea, J. A. K. Howard, and H. Puschmann, "OLEX2: a complete structure solution, refinement and analysis program," *Journal of Applied Crystallography*, vol. 42, no. 2, pp. 339–341, 2009.

[35] A. L. Niles, R. A. Moravec, and T. L. Riss, "Update on in vitro cytotoxicity assays for drug development," *Expert Opinion on Drug Discovery*, vol. 3, no. 6, pp. 655–669, 2008.

[36] S. Gama, F. Mendes, T. Esteves et al., "Synthesis and biological studies of pyrazolyl-diamine PtII complexes containing polyaromatic DNA-binding groups," *ChemBioChem*, vol. 13, no. 16, pp. 2352–2362, 2012.

[37] C. N. Pace, F. Vajdos, L. Fee, G. Grimsley, and T. Gray, "How to measure and predict the molar absorption coefficient of a protein," *Protein Science*, vol. 4, no. 11, pp. 2411–2423, 1995.

[38] B. Demoro, R. F. M. De Almeida, F. Marques et al., "Screening organometallic binuclear thiosemicarbazone ruthenium complexes as potential anti-tumour agents: cytotoxic activity and human serum albumin binding mechanism," *Dalton Transactions*, vol. 42, no. 19, pp. 7131–7146, 2013.

[39] B. Valeur and M. N. Berberan-Santos, *Molecular Fluorescence: Principles and Applications*, Wiley-VCH Verlag GMBh, Hoboken, NJ, USA, 2001.

[40] M. Serrano-Ruiz, C. Lidrissi, S. Mañas, M. Peruzzini, and A. Romerosa, "Synthesis, reactivity and catalytic properties of the allenylidene [Ru(CCCPh2)Cp(PTA)(PPh3)](CF3SO3) (PTA = 1,3,5-triaza-7-phosphaadamantane)," *Journal of Organometallic Chemistry*, vol. 751, pp. 654–661, 2014.

[41] S. D. Kirik, L. A. Solovyov, A. I. Blokhin, I. S. Yakimov, and M. L. Blokhina, "Structures and isomerization in diamminedichloropalladium(II)," *Acta Crystallographica Section B Structural Science*, vol. 52, no. 6, pp. 909–916, 1996.

[42] D. Y. Naumov, S. P. Khranenko, N. V. Kuratieva, A. V. Panchenko, and S. A. Gromilov, "New data on the structure of α-trans-[Pd(NH3)2Cl2]," *Journal of Structural Chemistry*, vol. 57, no. 8, pp. 1600–1605, 2017.

[43] N. Kordestani, H. Amiri Rudbari, I. Correia et al., "Heteroleptic enantiopure Pd(II)-complexes derived from halogen-substituted Schiff bases and 2-picolylamine: synthesis, experimental and computational characterization and investigation of the influence of chirality and halogen atoms on the anticancer activity," *New Journal of Chemistry*, vol. 45, no. 20, pp. 9163–9180, 2021.

[44] K. Singh, A. Gangrade, A. Jana, B. B. Mandal, and N. Das, "Design, synthesis, characterization, and antiproliferative activity of organoplatinum compounds bearing a 1,2,3-triazole ring," *ACS Omega*, vol. 4, no. 1, pp. 835–841, 2019.

[45] L. Côrte-Real, B. Karas, A. R. Brás et al., "Ruthenium-cyclopentadienyl bipyridine-biotin based compounds: synthesis and biological effect," *Inorganic Chemistry*, vol. 58, no. 14, pp. 9135–9149, 2019.

[46] R. G. Teixeira, A. R. Brás, L. Côrte-Real et al., "Novel ruthenium methylcyclopentadienyl complex bearing a bipyridine perfluorinated ligand shows strong activity towards colorectal cancer cells," *European Journal of Medicinal Chemistry*, vol. 143, pp. 503–514, 2018.

[47] L. Côrte-Real, F. Mendes, J. Coimbra et al., "Anticancer activity of structurally related ruthenium(II) cyclopentadienyl complexes," *Journal of Biological Inorganic Chemistry*, vol. 19, no. 6, pp. 853–867, 2014.

[48] B. Gonzalez, P. Lorenzo-Luis, A. Romerosa, M. Serrano-Ruiz, and P. Gili, "Theoretical aspects on water soluble [RuClCp(PPh3)2], [RuClCp(PTA)(PPh3)], [RuClCp(PTA)2], [RuClCp(mPTA)(PPh3)]+ and [RuClCp(mPTA)2]2+ (PTA = 1,3,5-triaza-7-phosphaadamantane; mPTA = N-methyl-1,3,5-triaza-7-phosphaadamantane)," *Journal of Molecular Structure: THEOCHEM*, vol. 894, no. 1-3, pp. 59–63, 2009.

[49] L. Côrte-Real, B. Karas, P. Gírio et al., "Unprecedented inhibition of P-gp activity by a novel ruthenium-cyclopentadienyl compound bearing a bipyridine-biotin ligand," *European Journal of Medicinal Chemistry*, vol. 163, pp. 853–863, 2019.

[50] B. Demoro, A. Bento-Oliveira, F. Marques et al., "Interaction with blood proteins of a ruthenium(II) nitrofuryl semicarbazone complex: effect on the antitumoral activity," *Molecules*, vol. 24, no. 16, p. 2861, 2019.

[51] R. Starosta, F. C. Santos, and R. F. M. de Almeida, "Human and bovine serum albumin time-resolved fluorescence: tryptophan and tyrosine contributions, effect of DMSO and rotational diffusion," *Journal of Molecular Structure*, vol. 1221, Article ID 128805, 2020.

[52] J. M. Beechem and L. Brand, "Time-resolved fluorescence of proteins," *Annual Review of Biochemistry*, vol. 54, no. 1, pp. 43–71, 1985.

[53] T. Otosu, E. Nishimoto, and S. Yamashita, "Multiple conformational state of human serum albumin around single tryptophan residue at various pH revealed by time-resolved fluorescence spectroscopy," *Journal of Biochemistry*, vol. 147, no. 2, pp. 191–200, 2010.

[54] J. R. Albani, "Origin of tryptophan fluorescence lifetimes part 1. Fluorescence lifetimes origin of tryptophan free in solution," *Journal of Fluorescence*, vol. 24, pp. 93–104, 2014.

[55] C. P. Matos, A. Valente, F. Marques et al., "New polydentate Ru(III)-Salan complexes: synthesis, characterization, antitumour activity and interaction with human serum proteins," *Inorganica Chimica Acta*, vol. 394, pp. 616–626, 2013.

[56] G. Colmenarejo, "In silico prediction of drug-binding strengths to human serum albumin," *Medicinal Research Reviews*, vol. 23, no. 3, pp. 275–301, 2003.

[57] J. Costa Pessoa and I. Tomaz, "Transport of therapeutic vanadium and ruthenium complexes by blood plasma components," *Current Medicinal Chemistry*, vol. 17, no. 31, pp. 3701–3738, 2010.

[58] J. Ghuman, P. A. Zunszain, I. Petitpas, A. A. Bhattacharya, M. Otagiri, and S. Curry, "Structural basis of the drug-binding specificity of human serum albumin," *Journal of Molecular Biology*, vol. 353, no. 1, pp. 38–52, 2005.

[59] D. V. Luís, J. Silva, A. I. Tomaz et al., "Insights into the mechanisms underlying the antiproliferative potential of a Co(II) coordination compound bearing 1,10-phenanthroline-5,6-dione: DNA and protein interaction studies," *Journal of Biological Inorganic Chemistry*, vol. 19, no. 6, pp. 787–803, 2014.

[60] A. M. De Matos, M. T. Blázquez-Sánchez, A. Bento-Oliveira et al., "Glucosylpolyphenols as inhibitors of aβ-induced fyn kinase activation and tau phosphorylation: synthesis, membrane permeability, and exploratory target assessment within the scope of type 2 diabetes and alzheimer's disease," *Journal of Medicinal Chemistry*, vol. 63, no. 20, pp. 11663–11690, 2020.

[61] L. M. S. Loura, R. F. M. De Almeida, A. Coutinho, and M. Prieto, "Interaction of peptides with binary phospholipid membranes: application of fluorescence methodologies," *Chemistry and Physics of Lipids*, vol. 122, no. 1-2, pp. 77–96, 2003.

[62] J. T. Marquês and R. F. M. de Almeida, "Application of ratiometric measurements and microplate fluorimetry to protein denaturation: an experiment for analytical and biochemistry students," *Journal of Chemical Education*, vol. 70, no. 5, pp. 1522–1527, 2013.